

Synergistic Effects of Fluorine and WO₃ Nanoparticles on the Surface of TiO₂ Hollow Spheres for Enhanced Photocatalytic Activity under Visible Light Irradiation

Dongyoon Shin,* Duk-Hee Lee, Chan-Gi Lee, and Kyung-Soo Park*

Cite This: *ACS Omega* 2021, 6, 30942–30948

Read Online

ACCESS |



Metrics & More

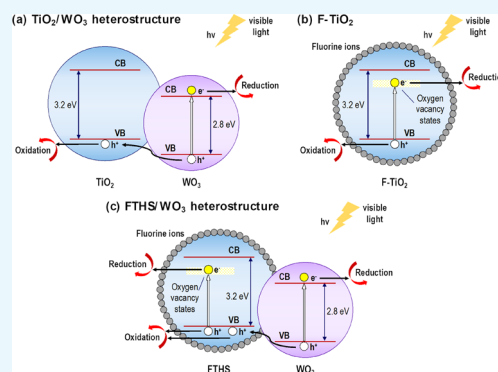


Article Recommendations



Supporting Information

ABSTRACT: TiO₂ is an attractive catalyst for the photocatalytic degradation of organic pollutants. However, owing to its large band gap, it can only be activated by ultraviolet (UV) light, which constitutes a small portion of solar energy. Therefore, there has been significant interest in extending its light absorption range from UV to visible light. In this study, fluorinated TiO₂ hollow spheres (FTHSs) were prepared via a rapid and simple wet chemical process using ammonium hexafluorotitanate, and then FTHS/WO₃ heterostructures with different weight ratios of the FTHS and WO₃ nanoparticles were synthesized via a simple wet impregnation method. The formation of the hybrid structure was confirmed by various characterization techniques. The photocatalytic activity of the synthesized photocatalysts in the photodegradation of rhodamine B, a model pollutant, was evaluated under visible light irradiation. The FTHS/WO₃ heterostructures exhibited significantly improved photocatalytic activity compared to the bare FTHS or WO₃ nanoparticles. The photodegradation efficiency of the FTHS/WO₃ heterostructure in the present study was up to 0.0581 min⁻¹. Detailed mechanisms that lead to the enhanced photocatalytic activity of the heterostructures are discussed. In addition, comparative experiments reveal that the photodegradation efficiency of the FTHS/WO₃ heterostructure under visible light irradiation is superior to that of the P25/WO₃ heterostructure prepared from the commercially available TiO₂ catalyst (P25) via the same impregnation method.



1. INTRODUCTION

Semiconductor-based photocatalysts have received much attention, especially owing to their applicability in the degradation of contaminants to remedy environmental issues.^{1–4} Diverse anthropogenic chemicals such as textile dyes and surfactants have contaminated the environment. Several studies have demonstrated that photocatalytic degradation is an effective method for treating these pollutants. Therefore, a wide range of semiconductor photocatalysts, such as TiO₂,^{5–7} WO₃,^{8–10} ZnO,^{11,12} and CuS,^{13,14} have been studied for the photocatalytic degradation of contaminants. Among these, TiO₂ is one of the most promising photocatalysts because of its favorable properties such as nontoxicity, chemical stability, and low cost. However, the photocatalytic performance of TiO₂-based photocatalysts needs to be improved further for their practical application.

Although TiO₂ is the most widely used semiconductor photocatalyst, it has a huge drawback. It has a relatively large band gap and can only be activated by ultraviolet (UV) light, which constitutes only about 3–5% of solar energy.¹⁵ Therefore, there has been great interest in extending its light absorption range from UV to visible light. Compared to TiO₂, WO₃ has a smaller band gap and has received great attention as a visible-light-driven photocatalyst. However, the conduction

band (CB) edge potential of WO₃ is more positive than the reduction potential of O₂, which is not favorable for the production of superoxide radicals and leads to low photocatalytic performance.⁸ Recently, many strategies have been proposed to improve the photocatalytic activities of TiO₂ and WO₃ photocatalysts. TiO₂ and WO₃ photocatalysts have been modified by coupling with cocatalysts^{5–7,16–18} or combining with other semiconductors^{2,19–26} to decrease the recombination of charge carriers and extend the light absorption range. For example, Li et al. reported that the 1T-WS₂/TiO₂/Ti₃C₂ composite with double metallic co-catalysts exhibited nearly 50 times higher photocatalytic H₂ evolution performance than TiO₂ nanosheets.⁵ Guo et al. showed that the carbon-coated TiO₂ nano-dendrites exhibited stronger photocatalytic hydrogen evolution performance than TiO₂ nanobelts under simulated solar light irradiation.⁶ Qin et al. used the gold nanorods to enhance the visible and near-infrared light

Received: June 20, 2021

Accepted: October 6, 2021

Published: November 11, 2021



absorption of TiO₂ and achieved the enhancement of full solar spectrum photocatalytic antibacterial properties.⁷ Among these methods, combining TiO₂ and WO₃ has attracted much attention because the TiO₂/WO₃ heterojunction facilitates improved charge separation and the heterostructure can be activated with visible light.^{27–31} Previously, TiO₂/WO₃ heterostructures have been reported to show enhanced photocatalytic activity under both UV and visible light irradiation.^{29–31}

The particle size and morphology of the photocatalysts play vital roles in their photocatalytic activity. Therefore, many attempts have been made to control the size and morphology of semiconductor photocatalysts to enhance their photocatalytic performance. Recently, many studies on semiconductor photocatalysts have shown that a variety of hierarchically nanostructured photocatalysts, including TiO₂ hollow spheres, exhibit improved photocatalytic performance owing to the larger surface area and higher number of internal pores that ensure more active sites and better charge separation.^{31–34}

The photocatalytic efficiency of semiconductor catalysts also depends on their surface properties such as the surface acidity, surface functional groups, defects, and crystalline phases.³⁵ Recently, fluorine-containing TiO₂ (F–TiO₂), such as fluorine-doped TiO₂ or fluorinated TiO₂, has been investigated for examining the effect of fluorine on the photocatalytic behavior of TiO₂.^{34–38} F–TiO₂ showed significantly improved photocatalytic activity than that of bare TiO₂ owing to the creation of oxygen vacancies, enhancement of the surface acidity, and increase in the number of active sites.³⁷ In addition, the creation of oxygen vacancies also led to photocatalysis under visible light irradiation.³⁷

In our previous study, fluorinated TiO₂ hollow spheres (FTHSs) synthesized in a one-pot synthesis showed enhanced photocatalytic activity under UV light irradiation.³⁴ In the present study, FTHS and WO₃ nanoparticles were combined for the photodegradation of rhodamine B (RhB) under visible light irradiation and the FTHS/WO₃ heterostructure exhibited highly efficient photocatalysis under visible light irradiation owing to synergistic effects from the surface fluorination, hollow structure, and TiO₂/WO₃ heterojunction. The FTHS was prepared by a rapid and simple wet chemical process using ammonium hexafluorotitanate (AHFT) and boric acid, according to a method reported previously by us.³⁴ Then, FTHS/WO₃ heterostructures with different weight ratios of the FTHS and WO₃ nanoparticles were prepared via a simple wet impregnation method. The hybrid structure of the synthesized photocatalysts was confirmed by X-ray diffraction (XRD), field-emission scanning electron microscopy (FESEM), transmission electron microscopy (TEM), and X-ray photoelectron spectroscopy (XPS). Furthermore, the photocatalytic activity of the synthesized photocatalysts was evaluated with the photodegradation of RhB, as a model contaminant, under visible light irradiation. Although a few studies on the photocatalytic activity of TiO₂/WO₃ heterostructures under visible light irradiation have been reported, to the best of our knowledge, no study has been reported on the FTHS/WO₃ heterostructure. The obtained FTHS/WO₃ heterostructures exhibited significantly improved photocatalytic activity compared to the individual FTHS or WO₃ nanoparticles. The photodegradation efficiency of the FTHS/WO₃ heterostructures in the present study was up to 0.0581 min⁻¹. Moreover, additional experiments performed with P25,

a commercially available TiO₂ photocatalyst, as a reference material revealed that the photocatalytic activity of the FTHS/WO₃ heterostructure is superior to that of the P25/WO₃ heterostructure prepared via the same impregnation method.

2. MATERIALS AND METHODS

2.1. Materials. AHFT [(NH₄)₂TiF₆, China], boric acid (H₃BO₃, Daejung, Korea), formic acid (CH₂O₂, Daejung, Korea), WO₃ nanoparticles (Sigma-Aldrich, USA), P25 (TiO₂, Evonik, Germany), and RhB (C₂₈H₃₁ClN₂O₃, Sigma-Aldrich, USA) were used as received, without further purification.

2.2. Preparation of the FTHS. The FTHS was prepared by a rapid and simple wet chemical process using AHFT and boric acid, according to a previously reported method.³⁴ First, deionized water and formic acid were mixed at the same volume. Then, AHFT (10 g/L) and boric acid (10 g/L) were dissolved separately in equal amounts of this aqueous formic acid solution. Thereafter, each solution was heated and held at 90 °C for 5 min under constant stirring. The heated boric acid solution was then poured into the heated AHFT solution, and then a milky suspension formed. This suspension was held at 90 °C for 15 min without stirring. The resulting white precipitate was collected and washed several times with distilled water and ethanol. Finally, the obtained powder was dried in an oven at 70 °C for 6 h.

2.3. Synthesis of FTHS/WO₃ Heterostructures. FTHS/WO₃ heterostructures with different weight ratios of FTHS and WO₃ nanoparticles were synthesized via a simple wet impregnation method as follows: FTHS and WO₃ nanoparticles were mixed in ethanol at different weight ratios (FTHS/WO₃ = 9:1, 7:3, 5:5, 3:7, and 1:9). Each suspension was then heated and held at 70 °C to evaporate the solvent under constant stirring. Finally, the obtained powders were dried in an oven at 70 °C for 6 h.

2.4. Characterization. The morphology and elemental composition of the as-synthesized photocatalysts were analyzed by FESEM (JSM-6700F, JEOL, Japan) and high-resolution TEM (JEM-2100F, JEOL, Japan) along with energy-dispersive X-ray (EDX) spectrometry. The phase composition of the photocatalysts was analyzed by XRD (XRD-6100F, Shimadzu, Japan). The surface elemental states of the photocatalysts were analyzed by XPS (ESCALAB 250, Thermo Scientific, USA). The photocatalytic degradation of the organic contaminant was studied by UV–visible spectroscopy (JASCO V-730, USA).

2.5. Evaluation of the Photocatalytic Activity. To evaluate the photocatalytic activities of the as-synthesized photocatalysts, RhB was used as an organic pollutant. The photocatalytic degradation of aqueous RhB solution was carried out under visible light irradiation. For the evaluation, 0.05 g of the photocatalyst was added to 100 mL of an aqueous RhB solution (1 × 10⁻⁵ M). Before irradiation, the suspension was continuously stirred in the dark for 1 h to achieve adsorption–desorption equilibrium between RhB and the photocatalyst. Thereafter, the suspension was irradiated with visible light from a 200 W xenon lamp (XP 500VA, DY Tech Co., Korea) equipped with a longpass filter (>420 nm), which blocks UV wavelengths and transmits the visible light. Then, 4 mL aliquots of the suspension were collected at given time intervals, centrifuged, and analyzed by UV–vis spectroscopy. The concentration of RhB was determined from the intensity of the absorption peak at 554 nm.

3. RESULTS AND DISCUSSION

The crystallinity, morphology, and elemental composition of the synthesized FT HS were investigated by XRD, FESEM, TEM, and EDX. The XRD pattern of the FT HS (Figure S1) can be indexed to the anatase phase of TiO₂ (JCPDS no. 73-1674). It was free of any peaks related to other fluorine-containing phases. The FESEM (Figure S2a) and TEM (Figure S2b) images clearly reveal the hollow structure of the FT HS with a diameter of 400–600 nm and a shell thickness of 70–140 nm. TEM–EDX elemental mapping images (Figure S2c) show the uniform distribution of Ti, O, and F in the FT HS. These results indicate that the synthesized FT HS consists of FT HSs and that fluorine is not present in the TiO₂ crystal lattice. Furthermore, the surface chemistry of the FT HS was investigated by XPS (Figure S3). The wide-scan XPS profile presented in Figure S3a shows the photoelectron peaks of Ti 2p, F 1s, O 1s, and C 1s. Figure S3b shows the high-resolution XPS spectrum of the F 1s region. The F 1s peak at ~685 eV is assigned to the F anions physically adsorbed on the surface of the FT HS formed by the ligand–exchange reaction. Furthermore, the absence of any peak at 688 eV indicates the absence of F atoms of TiO_{2-x}F_x formed by the substitution of O in the TiO₂ crystal lattice with F.³⁶ The XPS results are consistent with the XRD (Figure S1) and TEM–EDX (Figure S2c) results. These XRD, TEM, EDX, and XPS results of the synthesized FT HS are in good agreement with those reported previously,³⁴ indicating the successful fabrication of the FT HS.

The crystallinity of the synthesized FT HS/WO₃ heterostructures with different FT HS/WO₃ weight ratios (9:1, 7:3, 5:5, 3:7, and 1:9) was investigated by XRD (Figure 1). The

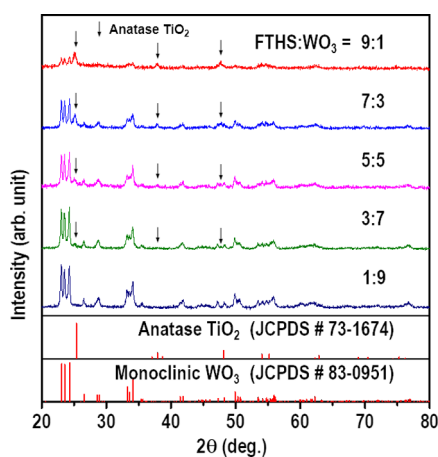


Figure 1. XRD patterns of FT HS/WO₃ heterostructures (FT HS/WO₃ = 9:1, 7:3, 5:5, 3:7, and 1:9).

XRD patterns of the FT HS/WO₃ heterostructures can be indexed to the anatase phase of TiO₂ (JCPDS no. 73-1674) and the monoclinic phase of WO₃ (JCPDS no. 83-0951). The intensity of the TiO₂ and WO₃ peaks increased/decreased according to their content in the heterostructure. In the case of the heterostructure with 1:9 FT HS/WO₃, the TiO₂ peaks did not appear because the amount of anatase TiO₂ is below the detection limit of the diffractometer.

The morphologies of the FT HS/WO₃ heterostructures, bare FT HS, and bare WO₃ nanoparticles were further investigated by FESEM, TEM, and EDX. Figure S4 shows the bare FT HS with a diameter of 400–600 nm, bare WO₃ nanoparticles with

a particle size of 20–100 nm, and the FT HS/WO₃ heterostructures, in which the FT HS and WO₃ nanoparticles are dispersed according to their weight ratio. Figure 2 shows the more complex morphology and elemental composition of the 7:3 FT HS/WO₃ heterostructure. The FESEM (Figure 2a) and TEM (Figure 2b) images show the hollow structure of the FT HS dispersed with 20–60 nm WO₃ nanoparticles. The TEM–EDX elemental mapping images of the FT HS/WO₃ heterostructure (Figure 2c) confirm the coexistence of the FT HS and WO₃, consistent with the XRD results (Figure 1), and also indicate that FT HS and WO₃ nanoparticles are attached to each other. They clearly show the presence of the FT HS and the WO₃ nanoparticles, which are well-dispersed on the surface of the FT HS. Thus, these results confirm the successful preparation of the FT HS/WO₃ heterostructures.

The photodegradation of RhB under visible light irradiation was studied to evaluate the photocatalytic activity of the synthesized FT HS, FT HS/WO₃ heterostructures (FT HS/WO₃ = 9:1, 7:3, 5:5, 3:7, and 1:9), and WO₃ nanoparticles. Figure 3a shows the results of the photodegradation of RhB with the FT HS, FT HS/WO₃ heterostructures, and WO₃ nanoparticles under visible light irradiation, that is, C_t/C₀ versus the irradiation time, where C₀ and C_t are the initial concentration and concentration at time *t* of RhB, respectively; *t* is the irradiation time. Regardless of the FT HS/WO₃ ratio, all the FT HS/WO₃ heterostructures exhibited significantly higher photocatalytic activity compared to that of the bare FT HS or WO₃ nanoparticles. The photocatalytic degradation of RhB can be expressed as a pseudo-first-order reaction described as³⁹

$$\ln(C_t/C_0) = kt \quad (1)$$

where *k* is the apparent rate constant. Figure 3b shows the linear relationship between ln(C₀/C_t) and the irradiation time for the photodegradation of RhB. The 7:3 FT HS/WO₃ heterostructure exhibited the highest photocatalytic efficiency, and its apparent rate constant is 0.0581 min⁻¹. The amount (in percentage) of the RhB degraded after 30 min of irradiation is shown in Figure 3c. The bare WO₃ nanoparticles were almost inactive during 1 h of irradiation, whereas the bare FT HS facilitated 9.15% RhB degradation after 30 min of irradiation. Although it is generally believed that individually, bare TiO₂ and bare WO₃ are unsuitable as visible-light-driven photocatalysts,⁸ the surface modification of TiO₂ with fluorine may create oxygen vacancies, enhance the surface acidity, and increase the number of active sites, leading to improved photocatalytic activity under visible light irradiation.³⁷ The following order of the photodegradation efficiency (the apparent rate constant, the amount of RhB degraded after 30 min of irradiation) is observed: 7:3 (0.0581 min⁻¹, 80.28%) > 3:7 (0.0321 min⁻¹, 68.02%) > 9:1 (0.0284 min⁻¹, 55.28%) > 5:5 (0.0297 min⁻¹, 49.21%) > 1:9 (0.0097 min⁻¹, 25.73%) >> bare FT HS (0.0039 min⁻¹, 9.15%) >>> bare WO₃ nanoparticles (inactive). Based on the performance of the 7:3 FT HS/WO₃ heterostructure, which exhibited the best photocatalytic efficiency in the present study, it may be stated that the decrease in the ratio of the WO₃ nanoparticles (9:1 FT HS/WO₃) leads to less absorption of the visible light, whereas the decrease in the ratio of the FT HS (5:5 FT HS/WO₃) leads to fewer active sites on the surface of the photocatalyst. When the ratio of the FT HS decreased further from 5:5 to 3:7, the 3:7 FT HS/WO₃ heterostructure showed better performance. We can assume that the enhancement of photocatalytic activity originated from the surface fluorination and the hollow

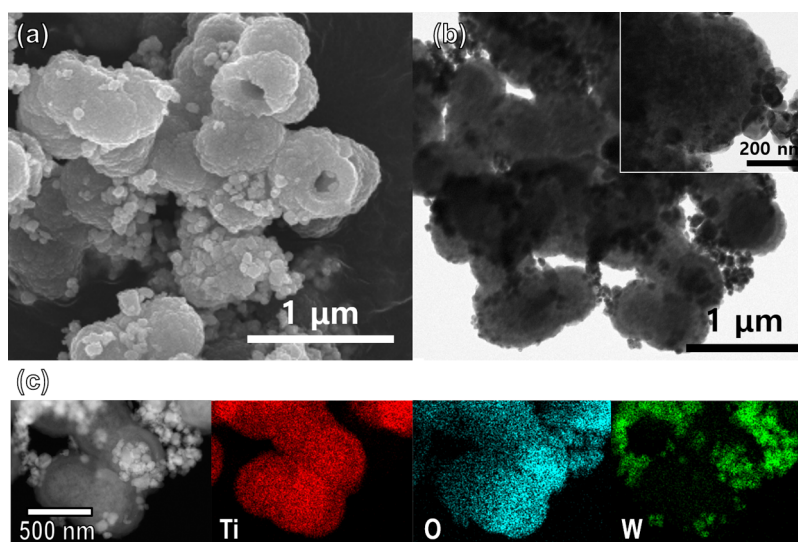


Figure 2. Microstructural characteristics of the FTHS/WO₃ heterostructure (FTHS/WO₃ = 7:3). (a) FESEM images, (b) TEM images, and (c) EDX elemental mapping images.

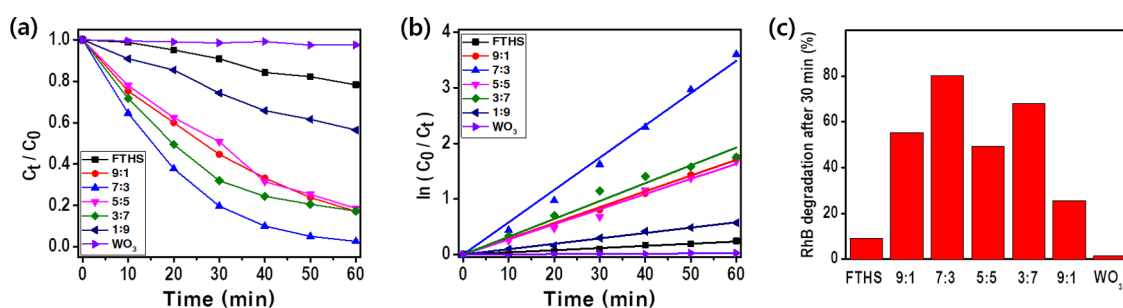


Figure 3. Photocatalytic activities of the FTHS, FTHS/WO₃ heterostructures (FTHS/WO₃ = 9:1, 7:3, 5:5, 3:7, and 1:9), and WO₃ nanoparticles under visible light irradiation. (a) Photocatalytic degradation of RhB, (b) first-order kinetics plot for the photocatalytic degradation of RhB, and (c) amount of RhB degraded after 30 min of irradiation.

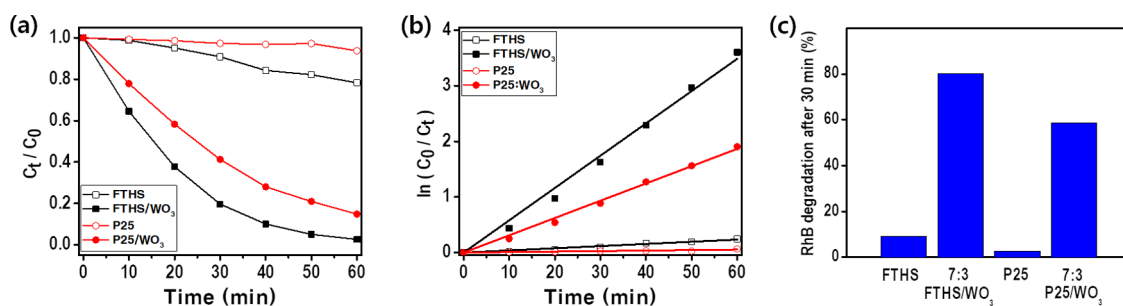


Figure 4. Photocatalytic activities of the FTHS, FTHS/WO₃ heterostructure (FTHS/WO₃ = 7:3), P25, and P25/WO₃ heterostructure (P25/WO₃ = 7:3) under visible light irradiation. (a) Photocatalytic degradation of RhB, (b) first-order kinetics plot for the photocatalytic degradation of RhB, and (c) amount of RhB degraded after 30 min of irradiation.

structure of the FTHS was maximized at the ratio of 7:3 and sharply declined with the decrease of the FTHS. However, the enhancement that originated from the TiO₂/WO₃ heterojunction inside the FTHS/WO₃ heterostructures was maximized at the ratio of 3:7 and remained at other ratios. In the present study, the FTHS/WO₃ ratio of 7:3 can be regarded as the optimal one for the photodegradation of RhB under visible light irradiation. The most critical reasons for the enhancement of the efficiency of the photocatalytic RhB degradation in the presence of the 7:3 FTHS/WO₃ heterostructure are as follows: (i) The surface fluorination and the TiO₂/WO₃ heterojunction may extend the absorption of light to the visible region and

decrease the recombination of photogenerated electrons and holes. (ii) In addition, the hollow structure may increase the surface area to improve the contact between the photocatalyst and RhB molecules.

Commercial P25, one of the most popular and the most active titania photocatalysts, was used as a reference sample to compare the photocatalytic activity of the optimal FTHS/WO₃ heterostructure. For an accurate experimental comparison, a 7:3 P25/WO₃ heterostructure was synthesized via the same impregnation method as that used for the FTHS/WO₃ heterostructure. The photodegradation of RhB under visible light irradiation was studied to evaluate the photocatalytic

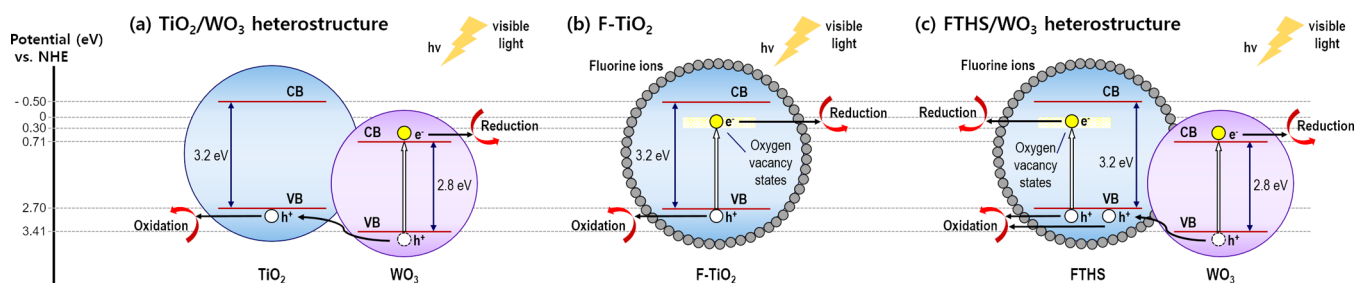


Figure 5. Schematic illustration of electron–hole pair separation and charge transfer under visible light irradiation in (a) TiO_2/WO_3 heterostructure, (b) F-TiO_2 , and (c) FTHS/WO_3 heterostructure, proposed in the present study.

activities of P25 and the synthesized 7:3 $\text{P25}/\text{WO}_3$ heterostructure. The results of the photodegradation of RhB on the FTHS, 7:3 FTHS/WO_3 heterostructure, P25, and 7:3 $\text{P25}/\text{WO}_3$ heterostructure in Figure 4a reveal that P25 is almost inactive during 1 h, whereas the photocatalytic activity of the 7:3 FTHS/WO_3 heterostructure is superior to that of the 7:3 $\text{P25}/\text{WO}_3$ heterostructure. Figure 4b shows the linear relationship between $\ln(C_0/C_t)$ and the irradiation time in the photodegradation of RhB with the 7:3 $\text{P25}/\text{WO}_3$ heterostructure. The apparent rate constant for the reaction on the 7:3 $\text{P25}/\text{WO}_3$ heterostructure is 0.0311 min^{-1} , which is approximately 1.9 times lower than that on the 7:3 FTHS/WO_3 heterostructure. Figure 4c shows the amount (in percentage) of RhB degraded after 30 min of irradiation. The amount of RhB degraded after 30 min of irradiation in the presence of the 7:3 $\text{P25}/\text{WO}_3$ heterostructure is 58.73%, which is approximately 1.4 times smaller than that observed with the 7:3 FTHS/WO_3 heterostructure. The following order of photodegradation efficiency (apparent rate constant, amount of RhB degraded after 30 min of irradiation) was observed: 7:3 FTHS/WO_3 (0.0581 min^{-1} , 80.28%) > 7:3 $\text{P25}/\text{WO}_3$ (0.0311 min^{-1} , 58.73%) \gg bare FTHS (0.0039 min^{-1} , 9.15%) \gg bare P25 (inactive). These results indicate that combining P25 with WO_3 nanoparticles led to significantly improved photocatalytic activity under visible light irradiation, similar to the case of the FTHS/WO_3 heterostructure. In addition, the FTHS/WO_3 heterostructure can be regarded as a better candidate than the $\text{P25}/\text{WO}_3$ heterostructure for visible-light-driven photocatalysis. This may be due to the advantages of the hollow structure and surface fluorination of the FTHS, which create oxygen vacancies, enhance the surface acidity, increase the number of active sites, and reduce the charge recombination.

The typical mechanisms for the photocatalytic degradation of RhB on the TiO_2/WO_3 heterostructure and F-TiO_2 are shown in Figure 5a,b, respectively. In the case of the TiO_2/WO_3 heterostructure (Figure 5a), WO_3 is activated by visible light, whereas TiO_2 is not. Electrons of WO_3 may be promoted from the valence band (VB) to the CB. As the VB edge potential of TiO_2 is more negative than that of WO_3 , the photogenerated holes in the VB of WO_3 may be transferred to the VB of TiO_2 .³¹ This decreases the photogenerated electron–hole recombination and enables more electrons and holes to be consumed in the reduction and oxidation reactions, respectively, at the surface of the photocatalyst. As a result, both the reduction and oxidation reactions produce hydroxyl radicals, which are very strong oxidants that decompose the RhB molecules. In the case of F-TiO_2 (Figure 5b), oxygen vacancies created by surface modification with fluorine, such as surface fluorination or fluorine doping, create oxygen vacancy states between the VB and CB of TiO_2 .³⁷ This may lead to a

new photoexcitation process in which electrons can be excited from the VB to the oxygen vacancy states under visible light irradiation; thus, the photogenerated electrons and holes can be consumed in the reduction and oxidation reactions, respectively. In the present study, the FTHS/WO_3 heterostructure can simultaneously facilitate both the aforementioned mechanisms (Figure 5a,b), as shown in Figure 5c. Therefore, these mechanisms result in considerable synergy that significantly enhances the photocatalytic activity under visible light irradiation.

Consequently, the surface fluorination, hollow structure, and TiO_2/WO_3 heterojunction led to beneficial effects, such as improving the separation of photogenerated electron–hole pairs, with completely different mechanisms, and thus, the synergy is amplified. In the present study, the 7:3 FTHS/WO_3 heterostructure showed the best performance in the photocatalytic degradation of RhB with an apparent rate constant of 0.0581 min^{-1} . This system is highly likely to exhibit further enhanced photocatalytic performance when combined with cocatalysts; for example, a variety of TiO_2 -based or WO_3 -based photocatalysts have been recently reported to show enhanced photocatalytic activity upon coupling with noble metals such as Pt, Au, and Ag.^{6,16–18} In addition, the FTHS/WO_3 heterostructure can be reasonably expected to show excellent photocatalytic performance under sunlight because as reported earlier, the FTHS exhibits high photocatalytic efficiency under UV light irradiation.³⁴ The facile synthesis and remarkable photocatalytic performance of the FTHS/WO_3 heterostructure suggest a realistic prospect of using them in the treatment of various environmental pollutants, such as dyes, surfactants, and phenols, and show their enormous potential for other applications, including water splitting and energy conversion.

4. CONCLUSIONS

In summary, we successfully synthesized FTHSs via a rapid and simple wet chemical process using AHFT. Then, we prepared FTHS/WO_3 heterostructures with different FTHS/ WO_3 weight ratios (9:1, 7:3, 5:5, 3:7, and 1:9) via a simple wet impregnation method. The photodegradation of RhB under visible light irradiation was investigated to compare the photocatalytic activities of the prepared heterostructures. The FTHS/WO_3 heterostructures exhibited significantly improved photocatalytic activities compared to those of the bare FTHS or WO_3 nanoparticles. The 7:3 FTHS/WO_3 heterostructure showed the best activity in the present study, and its apparent rate constant of RhB degradation is 0.0581 min^{-1} , which is, to the best of our knowledge, at the highest level for a TiO_2 -based or WO_3 -based visible-light-driven photocatalyst. In addition, the photodegradation efficiency of the 7:3 FTHS/WO_3 heterostructure (0.0581 min^{-1}) under visible light irradiation

is superior to that of the 7:3 P2S/WO₃ heterostructure (0.0311 min⁻¹) prepared using the most popular commercial photocatalyst, P2S, via the same impregnation method as that used for the FTHS/WO₃ heterostructure.

■ ASSOCIATED CONTENT

SI Supporting Information

The Supporting Information is available free of charge at <https://pubs.acs.org/doi/10.1021/acsomega.1c03220>.

XRD pattern of the FTHS; microstructural characteristics of the FTHS (FESEM image, TEM images, and TEM–EDX elemental mapping images); XPS results of the FTHS (survey spectrum and high-resolution spectrum in the F 1s region, Ti 2p region, and O 1s region); and FESEM images of FTHS, FTHS/WO₃ heterostructures, and WO₃ nanoparticles (PDF)

■ AUTHOR INFORMATION

Corresponding Authors

Kyung-Soo Park – Material Science & Chemical Engineering Center, Institute for Advanced Engineering (IAE), Yongin 175-28, Republic of Korea; Phone: +82-31-330-7422; Email: kspark@iae.re.kr; Fax: +82-31-330-7116

Dongyoon Shin – Material Science & Chemical Engineering Center, Institute for Advanced Engineering (IAE), Yongin 175-28, Republic of Korea; Institute for Physical Science and Technology and Department of Physics, University of Maryland, College Park, Maryland 20742, United States; orcid.org/0000-0003-2972-7513; Email: dyshin@umd.edu, shindpaper@gmail.com

Authors

Duk-Hee Lee – Material Science & Chemical Engineering Center, Institute for Advanced Engineering (IAE), Yongin 175-28, Republic of Korea

Chan-Gi Lee – Material Science & Chemical Engineering Center, Institute for Advanced Engineering (IAE), Yongin 175-28, Republic of Korea

Complete contact information is available at:

<https://pubs.acs.org/10.1021/acsomega.1c03220>

Notes

The authors declare no competing financial interest.

■ ACKNOWLEDGMENTS

This study was supported by the Korea Institute for Advancement of Technology (World class 300 R&D project), which is being funded by the Ministry of Trade, Industry and Energy, Republic of Korea (no. P0012996).

■ REFERENCES

- (1) Reddy, P. A. K.; Reddy, P. V. L.; Kwon, E.; Kim, K.-H.; Akter, T.; Kalagara, S. Recent advances in photocatalytic treatment of pollutants in aqueous media. *Environ. Int.* **2016**, *91*, 94–103.
- (2) Wang, H.; Zhang, L.; Chen, Z.; Hu, J.; Li, S.; Wang, Z.; Liu, J.; Wang, X. Semiconductor heterojunction photocatalysts: design, construction, and photocatalytic performances. *Chem. Soc. Rev.* **2014**, *43*, S234–S244.
- (3) Xu, Q.; Zhang, L.; Yu, J.; Wageh, S.; Al-Ghamdi, A. A.; Jaroniec, M. Direct Z-scheme photocatalysts: Principles, synthesis, and applications. *Mater. Today* **2018**, *21*, 1042–1063.

- (4) Chen, D.; Ray, A. Removal of toxic metal ions from wastewater by semiconductor photocatalysis. *Chem. Eng. Sci.* **2001**, *56*, 1561–1570.

- (5) Li, Y.; Ding, L.; Yin, S.; Liang, Z.; Xue, Y.; Wang, X.; Cui, H.; Tian, J. Photocatalytic H₂ evolution on TiO₂ assembled with Ti₃C₂ MXene and metallic 1T-WS₂ as co-catalysts. *Nano-Micro Lett.* **2020**, *12*, 6.

- (6) Guo, Y.; Kong, X.; Liang, Z.; Xue, Y.; Cui, H.; Tian, J. Non-high temperature method to synthesize carbon coated TiO₂ nanodendrites for enhanced wide spectrum photocatalytic hydrogen evolution activity. *J. Colloid Interface Sci.* **2020**, *571*, 412–418.

- (7) Qin, Y.; Guo, Y.; Liang, Z.; Xue, Y.; Zhang, X.; Yang, L.; Tian, J. Au nanorods decorated TiO₂ nanobelts with enhanced full solar spectrum photocatalytic antibacterial activity and the sterilization file cabinet application. *Chin. Chem. Lett.* **2021**, *32*, 1523–1526.

- (8) Abe, R.; Takami, H.; Murakami, N.; Ohtani, B. Pristine simple oxides as visible light driven photocatalysts: highly efficient decomposition of organic compounds over platinum-loaded tungsten oxide. *J. Am. Chem. Soc.* **2008**, *130*, 7780–7781.

- (9) Xi, G.; Ye, J.; Ma, Q.; Su, N.; Bai, H.; Wang, C. In situ growth of metal particles on 3D urchin-like WO₃ nanostructures. *J. Am. Chem. Soc.* **2012**, *134*, 6508–6511.

- (10) Wicaksana, Y.; Liu, S.; Scott, J.; Amal, R. Tungsten trioxide as a visible light photocatalyst for volatile organic carbon removal. *Molecules* **2014**, *19*, 17748–17762.

- (11) Singh, J.; Rathi, A.; Rawat, M.; Kumar, V.; Kim, K.-H. The effect of manganese doping on structural, optical, and photocatalytic activity of zinc oxide nanoparticles. *Compos. B Eng.* **2019**, *166*, 361–370.

- (12) Tian, C.; Zhang, Q.; Wu, A.; Jiang, M.; Liang, Z.; Jiang, B.; Fu, H. Cost-effective large-scale synthesis of ZnO photocatalyst with excellent performance for dye photodegradation. *Chem. Commun.* **2012**, *48*, 2858–2860.

- (13) Xu, W.; Zhu, S.; Liang, Y.; Li, Z.; Cui, Z.; Yang, X.; Inoue, A. Nanoporous CuS with excellent photocatalytic property. *Sci. Rep.* **2016**, *5*, 18125.

- (14) Tanveer, M.; Cao, C.; Aslam, I.; Ali, Z.; Idrees, F.; Khan, W. S.; Tahir, M.; Khalid, S.; Nabi, G.; Mahmood, A. Synthesis of CuS flowers exhibiting versatile photocatalyst response. *New J. Chem.* **2015**, *39*, 1459–1468.

- (15) Yu, J.; Qi, L. Template-free fabrication of hierarchically flower-like tungsten trioxide assemblies with enhanced visible-light-driven photocatalytic activity. *J. Hazard. Mater.* **2009**, *169*, 221–227.

- (16) Lee, S. Y.; Kang, D.; Jeong, S.; Do, H. T.; Kim, J. H. Photocatalytic Degradation of Rhodamine B Dye by TiO₂ and Gold Nanoparticles Supported on a Floating Porous Polydimethylsiloxane Sponge under Ultraviolet and Visible Light Irradiation. *ACS Omega* **2020**, *5*, 4233–4241.

- (17) Woo, S. H.; Kim, W. W.; Kim, S. J.; Rhee, C. K. Photocatalytic behaviors of transition metal ion doped TiO₂ powder synthesized by mechanical alloying. *Mater. Sci. Eng., A* **2007**, *449–451*, 1151–1154.

- (18) Sun, H.; He, Q.; She, P.; Zeng, S.; Xu, K.; Li, J.; Liang, S.; Liu, Z. One-pot synthesis of Au@TiO₂ yolk-shell nanoparticles with enhanced photocatalytic activity under visible light. *J. Colloid Interface Sci.* **2017**, *505*, 884–891.

- (19) Kaur, A.; Umar, A.; Anderson, W. A.; Kansal, S. K. Facile synthesis of CdS/TiO₂ nanocomposite and their catalytic activity for ofloxacin degradation under visible illumination. *J. Photochem. Photobiol., A* **2018**, *360*, 34–43.

- (20) Chang, M.-J.; Cui, W.-N.; Liu, J.; Wang, K.; Du, H.-L.; Qiu, L.; Fan, S.-M.; Luo, Z.-M. Construction of novel TiO₂/Bi₄Ti₃O₁₂/MoS₂ core/shell nanofibers for enhanced visible light photocatalysis. *J. Mater. Sci. Technol.* **2020**, *36*, 97–105.

- (21) Chen, G.; Wang, Y.; Shen, Q.; Xiong, X.; Ren, S.; Dai, G.; Wu, C. Fabrication of TiO₂ nanofibers assembled by Bi₂WO₆ nanosheets with enhanced visible light photocatalytic activity. *Ceram. Int.* **2020**, *46*, 21304–21310.

- (22) Gao, Y.; Wang, T. Preparation of Ag₂O/TiO₂ nanocomposites by two-step method and study of its degradation of RHB. *J. Mol. Struct.* **2021**, *1224*, 129049.
- (23) Theerthagiri, J.; Senthil, R. A.; Malathi, A.; Selvi, A.; Madhavan, J.; Ashokkumar, M. Synthesis and characterization of CuS-WO₃ composite photocatalyst for enhanced visible light photocatalytic activity. *RSC Adv.* **2015**, *5*, 52718–52725.
- (24) Jin, J.; Yu, J.; Guo, D.; Cui, C.; Ho, W. A hierarchical Z-scheme CdS-WO₃ photocatalyst with enhanced CO₂ reduction activity. *Small* **2015**, *11*, 5262–5271.
- (25) Chatchai, P.; Murakami, Y.; Kishioka, S.-y.; Nosaka, A. Y.; Nosaka, Y. Efficient photocatalytic activity of water oxidation over WO₃/BiVO₄ composite under visible light irradiation. *Electrochim. Acta* **2009**, *54*, 1147–1152.
- (26) Yu, C.; Yang, K.; Shu, Q.; Yu, J. C.; Cao, F.; Li, X. Preparation of WO₃/ZnO composite photocatalyst and its photocatalytic performance. *Chin. J. Catal.* **2011**, *32*, 555–565.
- (27) Puddu, V.; Mokaya, R.; Li Puma, G. Novel one step hydrothermal synthesis of TiO₂/WO₃ nanocomposites with enhanced photocatalytic activity. *Chem. Commun.* **2007**, 4749–4751.
- (28) Wang, C.; Zhang, X.; Yuan, B.; Wang, Y.; Sun, P.; Wang, D.; Wei, Y.; Liu, Y. Multi-heterojunction photocatalysts based on WO₃ nanorods: Structural design and optimization for enhanced photocatalytic activity under visible light. *Chem. Eng. J.* **2014**, *237*, 29–37.
- (29) Singh, S. A.; Madras, G. Photocatalytic degradation with combustion synthesized WO₃ and WO₃-TiO₂ mixed oxides under UV and visible light. *Sep. Purif. Technol.* **2013**, *105*, 79–89.
- (30) Smith, W.; Wolcott, A.; Fitzmorris, R. C.; Zhang, J. Z.; Zhao, Y. Quasi-core-shell TiO₂/WO₃ and WO₃/TiO₂ nanorod arrays fabricated by glancing angle deposition for solar water splitting. *J. Mater. Chem.* **2011**, *21*, 10792–10800.
- (31) Lv, K.; Li, J.; Qing, X.; Li, W.; Chen, Q. Synthesis and photo-degradation application of WO₃/TiO₂ hollow spheres. *J. Hazard. Mater.* **2011**, *189*, 329–335.
- (32) Tang, Y.; Wee, P.; Lai, Y.; Wang, X.; Gong, D.; Kanhere, P. D.; Lim, T.-T.; Dong, Z.; Chen, Z. Hierarchical TiO₂ nanoflakes and nanoparticles hybrid structure for improved photocatalytic activity. *J. Phys. Chem. C* **2012**, *116*, 2772–2780.
- (33) Chen, D.; Ye, J. Hierarchical WO₃ hollow shells: dendrite, sphere, dumbbell, and their photocatalytic properties. *Adv. Funct. Mater.* **2008**, *18*, 1922–1928.
- (34) Lee, D.-H.; Park, K.-S.; Lee, C.-G.; Swain, B. Facile one-pot synthesis of surface-fluorinated TiO₂ hollow spheres with enhanced photocatalytic activity. *J. Photochem. Photobiol., A* **2020**, *400*, 112654.
- (35) Park, H.; Choi, W. Effects of TiO₂ surface fluorination on photocatalytic reactions and photoelectrochemical behaviors. *J. Phys. Chem. B* **2004**, *108*, 4086–4093.
- (36) Yu, J. C.; Yu, J.; Ho, W.; Jiang, Z.; Zhang, L. Effects of F⁻ doping on the photocatalytic activity and microstructures of nanocrystalline TiO₂ powders. *Chem. Mater.* **2002**, *14*, 3808–3816.
- (37) Li, D.; Haneda, H.; Hishita, S.; Ohashi, N.; Labhsetwar, N. K. Fluorine-doped TiO₂ powders prepared by spray pyrolysis and their improved photocatalytic activity for decomposition of gas-phase acetaldehyde. *J. Fluor. Chem.* **2005**, *126*, 69–77.
- (38) Lee, D.-H.; Swain, B.; Shin, D.; Ahn, N.-K.; Park, J.-R.; Park, K.-S. One-pot wet chemical synthesis of fluorine-containing TiO₂ nanoparticles with enhanced photocatalytic activity. *Mater. Res. Bull.* **2019**, *109*, 227–232.
- (39) Chen, D.; Ray, A. K. Photodegradation kinetics of 4-nitrophenol in TiO₂ suspension. *Water Resour.* **1998**, *32*, 3223–3234.